September, 2012

Analysis of the spectra of trivalent erbium in multiple sites of hexagonal aluminum nitride

John B Gruber, *University of Texas at San Antonio*
Ulrich Vetter
Gary W Burdick, *Andrews University*
Zachery D Fleishman
Larry D Merkle, et al.

Analysis of the spectra of trivalent erbium in multiple sites of hexagonal aluminum nitride

John B. Gruber,[1] Ulrich Vetter,[2,*] Gary W. Burdick,[3] Zackery D. Fleischman,[4] Larry D. Merkle,[4] Takashi Taniguchi,[5] Yuan Xiaoli,[5] Takashi Sekiguchi,[5] Daniel Jürgens,[2] and Hans Hofsäss[2]

[1]*Department of Physics and Astronomy, The University of Texas at San Antonio, San Antonio, Texas 78249, USA*
[2]*II. Physikalisches Institut, Georg-August Universität Göttingen, Friedrich-Hund-Platz 1, 37077 Göttingen, Germany*
[3]*Department of Physics, Andrews University, Berrien Springs, Michigan 49104, USA*
[4]*U. S. Army Research Laboratory, RDRL SEE M, 2800 Powder Mill Road, Adelphi, Maryland 20783, USA*
[5]*National Institute for Materials Science, Namiki 1-1, Tsukuba Ibaraki 305-0044, Japan*
**uvetter@uni-goettingen.de*

Abstract: The 12 K cathodoluminescence spectra of Er^{3+} doped into single crystals of aluminum nitride (2H-AlN) in the hexagonal phase are reported between 320 nm and 775 nm. The emission spectra represent transitions from the lower Stark level of $^2P_{3/2}$ to the Stark levels of the $^4I_{15/2}$, $^4I_{13/2}$, $^4I_{11/2}$, $^4I_{9/2}$, $^4F_{9/2}$, and $^4S_{3/2}$ multiplet manifolds of $Er^{3+}(4f^{11})$. Emission spectra from $^4S_{3/2}$ to $^4I_{15/2}$ are also reported. All observed strong line emission are accounted for in terms of two principle sites, denoted site "a" and site "b", with a few line spectra attributed to additional sites. A parameterized Hamiltonian that includes the atomic and crystal-field terms for $Er^{3+}(4f^{11})^{2S+1}L_J$ was used to determine the symmetry and the crystal field splitting of the "a" and "b" sites. A descent in symmetry calculation was carried out to determine if distortion due to the size difference between Er, Al and the vacancies can be discerned. Modeling results assuming C_{3v} and C_{1h} are discussed. It appears that the sensitivity to a C_{1h} model is not sufficient to invalidate the choice of C_{3v} as an approximate symmetry for both sites. The g-factors reported from an EPR study of Er^{3+} in single-crystal AlN are in reasonable agreement with calculated g-factors for Er^{3+} in the "a" site assuming C_{3v} symmetry.

OCIS codes: (160.2540) Fluorescent and luminescent materials; (020.6580) Stark effect.

References and links

1. H. Ennen, J. Schneider, G. Pomrenke, and A. Axmann, "1.54-μm luminescence of erbium-implanted III-V semiconductors and silicon," Appl. Phys. Lett. **43**(10), 943–945 (1983).
2. S. M. Sze, *Semiconducting Devices, Physics and Technology* (Wiley, 1985).
3. W. Koechner, *Solid State Laser Engineering*, 5th ed. (Springer, 1999).
4. A. J. Steckl and J. M. Zavada, "Optoelectronic Properties and Applications of Rare-Earth-Doped GaN," MRS Bull. **24**, 33–38 (1999).
5. B. R. Judd, *Operator Techniques in Atomic Spectroscopy* (McGraw-Hill, 1963).
6. B. G. Wybourne, *Spectroscopic Properties of Rare-Earths* (Wiley, 1965).
7. G. Blasse and B. Granmaier, *Luminescent Materials* (Springer, 1994).
8. W. J. Tropf, M. E. Thomas, and T. J. Harris, "Properties of crystals and glasses," in *Handbook of Optics* (McGraw-Hill, 1995), Vol. 2.
9. R. Terao, J. Tatami, T. Meguro, and K. Komeya, "Fracture Behavior of AlN Ceramics with Rare Earth Oxides," J. Eur. Ceram. Soc. **22**(7), 1051–1059 (2002).
10. E. D. Readinger, G. D. Metcalfe, H. Shen, and M. Wraback, "GaN doped with neodymium by plasma-assisted molecular beam epitaxy," Appl. Phys. Lett. **92**(6), 061108 (2008).
11. N. Kuramoto and H. Taniguchi, "Transparent AlN ceramics," J. Mater. Sci. Lett. **3**(6), 471–474 (1984).
12. K. Lorenz, E. Alves, T. Monteiro, M. J. Soares, M. Peres, and P. J. M. Smulders, "Optical doping of AlN by rare earth implantation," Nucl. Instrum. Methods Phys. Res. B **242**(1–2), 307–310 (2006).
13. R. Maâlej, S. Kammoun, M. Dammak, and M. Kammoun, "Theoretical investigations of EPR parameters and local structure of single erbium center in hexagonal GaN layers," Mater. Sci. Eng. B **146**(1-3), 183–185 (2008).

#171375 - $15.00 USD Received 26 Jun 2012; revised 25 Jul 2012; accepted 27 Jul 2012; published 1 Aug 2012

14. S. Yang, S. M. Evans, L. E. Halliburton, G. A. Slack, S. B. Schujman, K. E. Morgan, R. T. Bondokov, and S. G. Mueller, "Electron paramagnetic resonance of Er^{3+} ions in aluminum nitride," J. Appl. Phys. **105**(2), 023714 (2009).
15. J. B. Gruber, G. W. Burdick, N. T. Woodward, V. Dierolf, S. Chandra, and D. K. Sardar, "Crystal-field analysis and Zeeman splittings of energy levels of Nd^{3+} ($4f^3$) in GaN," J. Appl. Phys. **110**(4), 043109 (2011).
16. L. D. Merkle, A. C. Sutorik, T. Sanamyan, L. K. Hussey, G. Gilde, C. Cooper, and M. Dubinskii, "Fluorescence of Er^{3+}:AlN polycrystalline ceramic," Opt. Mater. Express **2**(1), 78–91 (2012).
17. U. Vetter, J. Gruber, A. Nijjar, B. Zandi, G. Öhl, U. Wahl, B. De Vries, H. Hofsäss, and M. Dietrich; the ISOLDE Collaboration, "Crystal field analysis of Pm^{3+} ($4f^4$) and Sm^{3+} ($4f^5$) and lattice location studies of ^{147}Nd and ^{147}Pm in w-AlN," Phys. Rev. B **74**(20), 205201 (2006).
18. S. Petit, R. Jones, M. J. Shaw, P. R. Briddon, B. Hourahine, and T. Frauenheim, "Electronic behavior of rare-earth dopants in AlN: A density-functional study," Phys. Rev. B **72**(7), 073205 (2005).
19. T. Taniguchi, K. Watanabe, and A. Nakayama, "Synthesis of Eu-doped AlN crystals using Li-based Solvent Under High Pressure" (unpublished).
20. T. Taniguchi and K. Watanabe, "Synthesis of high-purity boron nitride single crystals under high pressure by using Ba–BN solvent," J. Cryst. Growth **303**(2), 525–529 (2007).
21. U. Vetter, H. Hofsäss, and T. Taniguchi, "Visible cathodoluminescence from Eu-implanted single- and polycrystal c-BN annealed under high-temperature, high-pressure conditions," Appl. Phys. Lett. **84**(21), 4286–4288 (2004).
22. R. Wyckhoff, *Crystal Structures,* 2nd ed. (Interscience, New York, 1965), Vol. 3.
23. N. Henry and K. Lonsdale, *International Tables for X-ray Crystallography* (Kynoch, 1952), Vol. 1.
24. J. B. Gruber, B. Zandi, H. J. Lozykowski, W. M. Jadwisienczak, and I. Brown, "Crystal-field splitting of Pr^{3+} ($4f^2$) energy levels in GaN," J. Appl. Phys. **89**(12), 7973–7976 (2001).
25. J. B. Gruber, B. Zandi, H. J. Lozykowski, and W. M. Jadwisienczak, "Spectroscopic properties of Sm^{3+} ($4f^5$) in GaN," J. Appl. Phys. **91**(5), 2929–2935 (2002).
26. J. B. Gruber, U. Vetter, H. Hofsäss, B. Zandi, and M. F. Reid, "Spectra and energy levels of Gd^{3+} ($4f^7$) in AlN," Phys. Rev. B **69**(19), 195202 (2004).
27. J. B. Gruber, U. Vetter, H. Hofsäss, B. Zandi, and M. F. Reid, "Spectra and energy levels of Tm^{3+} ($4f^{12}$) in AlN," Phys. Rev. B **70**(24), 245108 (2004).
28. J. B. Gruber, U. Vetter, T. Taniguchi, G. W. Burdick, H. Hofsäss, S. Chandra, and D. K. Sardar, "Spectroscopic analysis of Eu^{3+} in single-crystal hexagonal phase AlN," J. Appl. Phys. **110**(2), 023104 (2011).
29. W. T. Carnall, P. R. Fields, and K. Rajnak, "Spectral Intensities of the Trivalent Lanthanides and Actinides in Solution. II. Pm^{3+}, Sm^{3+}, Eu^{3+}, Gd^{3+}, Tb^{3+}, Dy^{3+}, and Ho^{3+}," J. Chem. Phys. **49**(10), 4412–4423 (1968).
30. W. T. Carnall, G. L. Goodman, K. L. Rajnak, and R. S. Rana, "A systematic analysis of the spectra of the lanthanides doped into single crystal LaF_3," J. Chem. Phys. **90**(7), 3443–3457 (1989).
31. J. B. Gruber, K. L. Nash, R. M. Yow, D. K. Sardar, U. V. Valiev, A. A. Uzokov, and G. W. Burdick, "Spectroscopic and magnetic susceptibility analyses of the ^7F_J and $^5D_4$ energy levels of Tb^{3+} ($4f^8$) in $TbAlO_3$," J. Lumin. **128**(8), 1271–1284 (2008).
32. J. B. Gruber, S. Chandra, D. K. Sardar, U. V. Valiev, N. I. Juraeva, and G. W. Burdick, "Modeling optical spectra and Van Vleck paramagnetism in Er^{3+}:$YAlO_3$," J. Appl. Phys. **105**(2), 023112 (2009).

1. Introduction

Interest in the detailed interpretation of the spectroscopic properties of wide band gap semiconductors such as the III-nitrides GaN and AlN doped with trivalent rare earth ions (RE^{3+}) has grown rapidly in recent years as the optoelectronic properties of these materials have been successfully exploited in photonic devices [1–4]. Within the band gap of AlN (approximately 6.1 eV), numerous sharp-line absorption and emission spectra of the RE^{3+} ions are observed due to transitions within the $4f^n$ subshell that is well shielded from the lattice by the filled $5s^2$ and $5p^6$ shells of the rare earth ion core [5–7]. The large optical window associated with hexagonal AlN is also transparent to the absorption and emission spectra arising from vacuum ultraviolet states of the RE^{3+} ions, transitions that are usually not observed in insulator hosts such as garnets, oxides and fluorides due to lattice absorption.

The physical properties of rare earth-doped AlN are attractive for purposes of application in that they have high fracture toughness, are relatively non-corrosive, and exhibit high thermal conductivity, although doping reduces the thermal conductivity somewhat [8,9]. Yet, the preparation and detailed optical characterization of the doped materials still provide challenges and opportunities that call for fundamental spectroscopic studies. The technologies of thin film, single crystal, and ceramic rare earth-doped AlN sample preparation and growth have improved greatly over recent years [10–12]. Experimental techniques that include specific wavelength laser excitation and up-conversion dynamics to probe observed multi-site

#171375 - $15.00 USD Received 26 Jun 2012; revised 25 Jul 2012; accepted 27 Jul 2012; published 1 Aug 2012

RE^{3+} spectra can be carried out to investigate local RE^{3+} site symmetries together with methods of electron spin resonance (EPR), Zeeman spectroscopy, and site-selective combined excitation and emission spectroscopy [13–15]. Because of the importance of Er^{3+} as an infrared laser, its upconversion capabilities, and its use in fiber-optic amplifiers by the communications industry, we have carried out the following detailed crystal-field splitting analysis of the multi-site spectra of Er^{3+} in single crystal AlN.

We begin by reporting the multi-site cathodoluminescence (CL) spectra of Er^{3+} in single-crystal hexagonal phase AlN obtained at 12 K between 320 nm and 775 nm. The spectra represent emission transitions from the lower energy (Stark) level of $Er^{3+}(4f^{11})$ $^2P_{3/2}$ to the Stark levels of the ground state, $^4I_{15/2}$, and excited multiplet manifolds $^4I_{13/2}$, $^4I_{11/2}$, $^4I_{9/2}$, $^4F_{9/2}$ and $^4S_{3/2}$. The CL spectra include transitions from both Stark levels of $^4S_{3/2}$ to $^4I_{15/2}$, which confirm the energy (Stark) level splitting of $^4I_{15/2}$. All observed strong, sharp spectra are accounted for by assuming transitions from two Er sites, which we designate as principle sites "a" and "b", with a few generally weak lines attributed to additional sites.

We also report refinements of the spectrofluorometric experiments and interpretation of Merkle *et al*. [16]. These site selection data identify most of the $^4I_{15/2}$, $^4I_{13/2}$, $^4I_{11/2}$ and $^4I_{9/2}$ energy levels for Er^{3+} in the principal "a" site in a ceramic Er:AlN sample, and confirm levels derived from the CL data. Thus, the site selection data guide the identification of lines associated with one principle site in the CL spectra.

Recent emission channeling experiments and lattice location studies of RE^{3+} in 2H-AlN by Vetter *et al*. [17] indicate that the main sites for RE^{3+} ions doped into hexagonal AlN occupy vacant cation (Al) sites, although a number of substitutional minority sites are found as well. Yang *et al*. [14], after reviewing possible local sites for Er^{3+} in single crystal hexagonal AlN, concluded that C_{3v} symmetry for Er^{3+} in a sample with a concentration of about 10^{16} cm^{-3} agreed with their EPR analysis. Such low RE^{3+} doping, however, precludes observation of the details of the weak $4f^{11}$ spectrum of Er^{3+}. A much larger concentration of Er^{3+} is needed to observe, analyze, and model the optical spectroscopy.

However, for larger amounts of Er^{3+}, the local site symmetry can be distorted during crystal growth since the radius of Er^{3+} is larger than the radius of the Al^{3+} it replaces. This causes stress on the surrounding environment. In fact, local-density functional modeling by Petit *et al*. [18] suggests that a neighboring oxygen ion or neighboring nitrogen vacancy next to Er^{3+} may substitute for a basal-plane N to form complexes such as Er^{3+}-O_N or Er^{3+}-V_N with C_{1h} symmetry. In effect, the Er^{3+} ions that occupy Al vacancies of C_{3v} symmetry may shift along the c-axis toward the basal plane into a site of C_{1h} symmetry in order to reduce the local stress associated with its size. Thus, the site symmetry of Er^{3+} in the present study could be C_{3v} or lower, possibly depending on the amount and distribution of Er^{3+} ions in the lattice.

To identify the appropriate symmetry, we performed descent in symmetry calculations from C_{3v} to C_3 (assuming the mirror plane symmetry is broken) and from C_{3v} to C_{1h} (assuming the mirror plane remains, but the three-fold rotation symmetry axis is broken). The crystal-field splitting of the energy levels of Er^{3+} in each site is modeled assuming each of these symmetries, as discussed in section 4.

2. Experimental details

Single crystals of hexagonal phase aluminum nitride (2H-AlN) doped with trivalent erbium were grown by a temperature gradient method under high temperature and high pressure [19] with the use of a belt-type high pressure, high temperature (HP-HT) apparatus designed to grow materials having similar physical crystalline properties [20,21]. Li_3AlN_2, together with $Ba_3Al_2N_4$, was used as the solvent. The solvent was mixed with ErF_3 and packed into a molybdenum sample chamber. Both steps were carried out under a dry nitrogen atmosphere. The assembled cell was then compressed to 6.5 GPa and heated to 1400 °C for 4.5 hours and quenched to room temperature by shutting off the heater power supply. The end product

#171375 - $15.00 USD Received 26 Jun 2012; revised 25 Jul 2012; accepted 27 Jul 2012; published 1 Aug 2012

resulted in lightly colored crystals with diameters up to 0.4 mm and a maximum size of less than 0.5 mm on a side parallel to the c-axis.

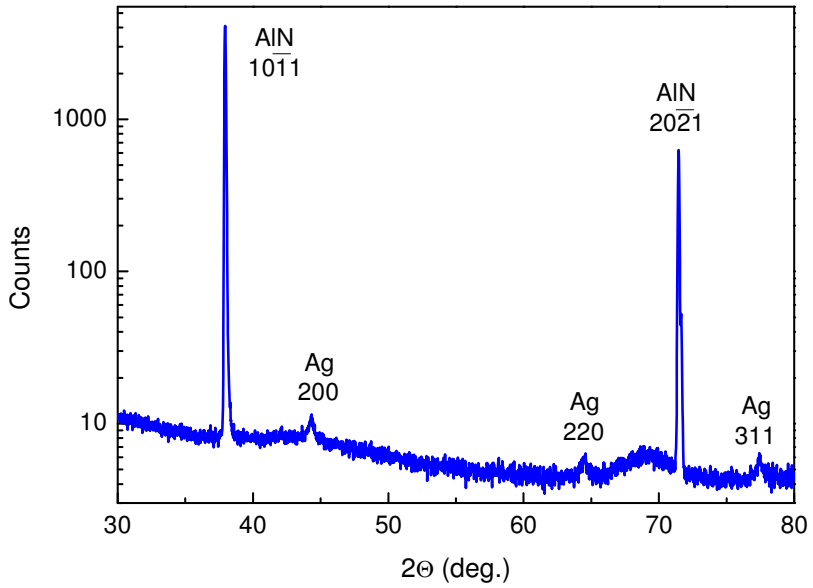

Fig. 1. The XRD pattern showing the hexagonal structure of AlN doped with Er^{3+}; conductive silver paste is used in supporting the samples.

The crystal structure was confirmed by x-ray diffraction (XRD) with a Bruker AXS D8 Advance, which is equipped with a Cu K-alpha x-ray source. Figure 1 shows a typical XRD pattern of the Er^{3+}-doped AlN crystals mounted on a silicon substrate using silver paste. None of the XRD measurements indicated the formation of any other phase, including rare-earth rich phases within the AlN crystals. The hexagonal structure (wurzite phase) of AlN was confirmed [22,23]. The space group is $C_{6v}^4(P6_3mc)$, with both Al and N occupying C_{3v} sites in the unit cell. Earlier emission channeling experiments [17] identify the location of the majority of RE^{3+} as substituting for Al^{3+} in cation vacancies, some of which may form complexes with nitrogen vacancies.

The CL spectra were obtained from crystals mounted on the head of a closed-cycle helium refrigerator positioned within a vacuum chamber. An electronically controlled calibrated resistive heater was maintained at a selected sample temperature while the spectra were recorded. The CL spectra were obtained at several temperatures from approximately 12 K to room temperature in order to record any temperature dependence in the spectra. A SPECS Eq. (22) Auger electron gun was used as the excitation source that produced electrons having energies between 100 eV and 5 keV and beam currents between 0.01μA and 150 μA. The CL spectra were produced by electrons excited to 5 keV with a beam current of 2 $\mu A/mm^2$. The emission was passed through a quartz window and a pair of UV-coated lenses before reaching the entrance slit of a 1.0 m Czerny-Turner spectrograph (Jobin-Yvon 1000M). The spectrograph was equipped with holographic gratings blazed at 250 nm with 1200 lines/mm and at 1000 nm with 600 lines/mm, and calibrated using a Hg arc standard. Resolution of the spectra was better than 0.05 nm for the sharpest transitions. Detection was carried out with a nitrogen-cooled CCD camera that recorded the spectra between 300 nm and 1000 nm. Uncertainty in the wavelength measurements was approximately 0.02 nm. The methods used to record the CL spectra are similar to the methods we reported earlier [24–28].

Site selection spectroscopy was performed on ceramic Er:AlN material, as exemplified in Fig. 2 and described in [16], using techniques very similar to those reported therein. Upgrades

#171375 - $15.00 USD Received 26 Jun 2012; revised 25 Jul 2012; accepted 27 Jul 2012; published 1 Aug 2012

to the optical cryostat facilitated measurements at temperatures both lower and higher than the 20 K at which most spectra in that work were taken. Fluorescence spectra were taken with spectral band pass as narrow as 0.3 nm, and excitation wavelengths could be selected to a typical specificity of 0.2 nm.

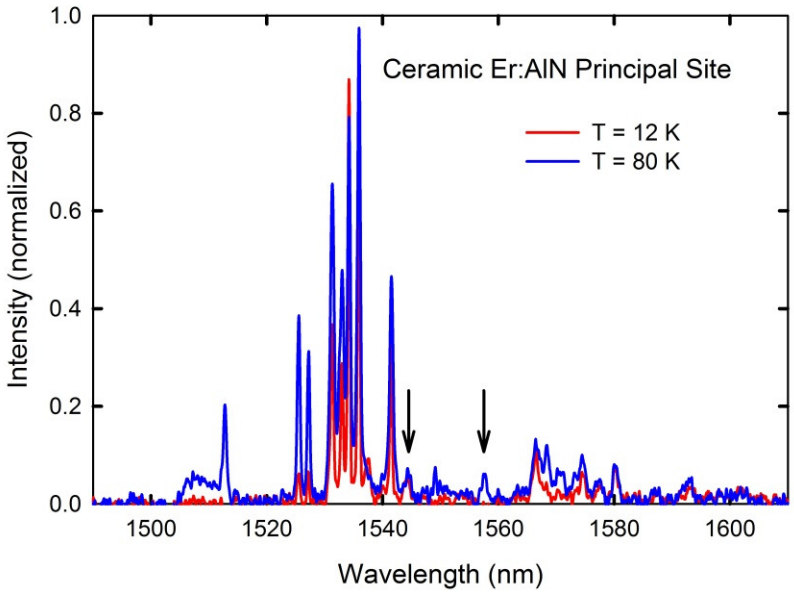

Fig. 2. Fluorescence of ceramic Er:AlN due to excitation of one of the principal site's absorption lines. The arrows indicate the peaks at about 1544.5 and 1558.25 nm, discussed in the text.

3. Data analysis

The multi-site CL spectral lines obtained at 12 K between 320 nm and 775 nm are listed in Table 1 (column 2) for $Er^{3+}(4f^{11})$ energy levels, including the ground state, $^4I_{15/2}$, and excited states $^4I_{13/2}$, $^4I_{11/2,}$ $^4I_{9/2}$, $^4F_{9/2}$, and $^4S_{3/2}$. Using empirical methods of energy differences between transition energies and temperature dependent peak characteristics, more than 97% of the spectra reported in column 2 can be accounted for in terms of two sites, with the remaining 3% of the spectra likely associated with other Er sites for which there is insufficient data for analysis. The transitions numbered in column 5 are identified as site "a" under cols. 6-8 and site "b" under cols. 9 and 10. Column 5 identifies the transition from the lower energy (Stark) level of $^2P_{3/2}$ to one of the J + 1/2 terminal Stark levels within each $^{2S+1}L_J$ multiplet manifold listed in column 1. The transition numbers also correspond to the emission peaks identified in Figs. 3 through 9.

The experimental Stark levels inferred from CL of the single crystal material may be compared with those inferred from site selection spectroscopy of the ceramic. To facilitate this comparison, higher resolution temperature-dependent measurements for selected excitation wavelengths have been used to refine the level assignments for the principal site reported in Merkle *et al*. [16]. The great majority of the assignments are confirmed, and are within one or two wave numbers of the originally reported values, as may be seen by comparing column 7 of Table 1 with [16]. In the case of the $^4I_{9/2}$ manifold, our new data shift the energy levels lower by as much as 6 cm^{-1}, but the splittings are only subtly changed. However, there are a few exceptions to this overall agreement, which can affect the assignment of levels in the CL data and the fitting of crystal field theory to the data.

#171375 - $15.00 USD Received 26 Jun 2012; revised 25 Jul 2012; accepted 27 Jul 2012; published 1 Aug 2012

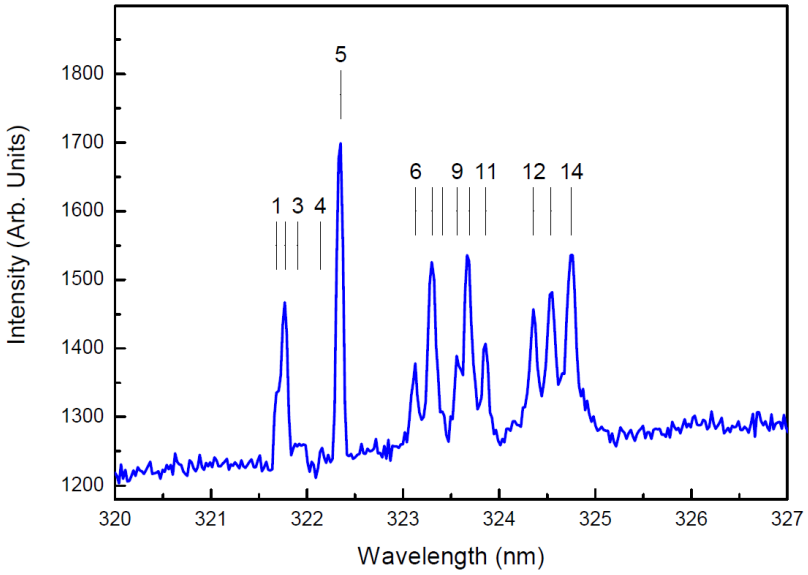

Fig. 3. The 12 K CL spectrum of Er^{3+} in AlN between 320 nm and 327 nm representing transitions from $^{2}P_{3/2}$ to $^{4}I_{15/2}$.

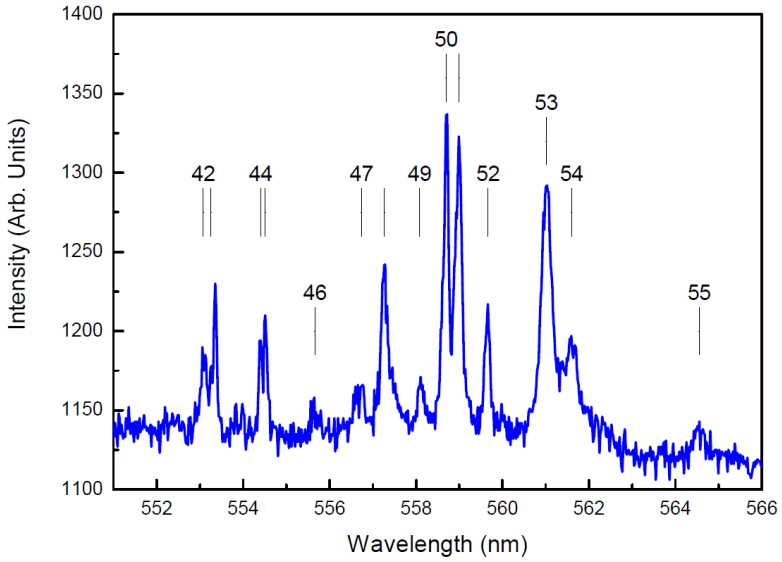

Fig. 4. The 12 K CL spectrum of Er^{3+} in AlN between 551 nm and 566 nm representing transitions from $^{4}S_{3/2}$ to $^{4}I_{15/2}$.

#171375 - $15.00 USD Received 26 Jun 2012; revised 25 Jul 2012; accepted 27 Jul 2012; published 1 Aug 2012

Table 1. CL spectrum (12 K) of Er:AlN from the lowest Stark component of $^2P_{3/2}$ at 31076 cm^{-1} (site "a") and 31069 cm^{-1} (site "b")[a]

					Site "a" final state (cm^{-1})			Site "b" final state(cm^{-1})	
$^{2S+1}L_J$	λ (nm)	Intensity (arb)	Energy (cm^{-1})	Trans. number	E_{exp}(CL)	E_{exp}(SS)	E_{calc}	E_{exp}(CL)	E_{calc}
$^4I_{15/2}$	321.7(s)	125	31076	1	0	0	-6		
	321.77	235	31069	2	7	7	9	0	0
	321.9(b)	65	31046	3	30	30	41		
	322.14	60	31033	4	43	43	56		
	322.35	460	31013	5				56	56
	323.13	115	30938	6	138	135	128	131	124
	323.30	290	30922	7				147	137
	323.4(s)	40	30913	8(na)					
	323.56	120	30897	9				172	174
	323.69	290	30885	10	191	189	180		
	323.86	120	30869	11				200	200
	324.19	180	30837	12	239	240	247	248	250
	324.54	195	30804	13	272	278	272		
	324.75	255	30784	14				285	300
$^4I_{13/2}$	407.05	260	24560	15	6516	6516	6512	6520	6518
	407.26	110	24548	16	6528	6529	6523		
	407.34	375	24543	17	6533	6538	6527		
	407.54	25	24531	18				6546	6551
	407.66	25	24523	19	6553	6553	6567		
	407.96	135	24505	20				6575	6580
	408.58	285	24468	21	6608	6608	6601	6601	6605
	408.86	1505	24451	21	6625	6632	6625	6618	6622
	409.07	500	24439	23				6630	6629
	409.33	265	24423	24(na)					
	409.74	245	24398	25	6677	6680	6664		
	410.04	345	24381	26				6688	6666
$^4I_{11/2}$	478.14	400	20909	27	10167	10150	10169	10164	10166
	478.36	1400	20899	28	10177	10170	10173	10185	10184
	478.54	500	20891	29	10185	10187	10181	10192	10198
	478.71	950	20884	30	10192	10193	10203	10209	10210
	479.10	950	20865	31	10211	10212	10216	10213	10213
	479.73	2910	20839	32	10237		10243	10230	10229
$^4I_{9/2}$	530.67	30(b)	18838	33	12238	12232	12229	12235	12233
	531.83	300	18797	34	12279	12277	12285		
	532.33	50	18780	35				12289	12301
	532.81	140	18762	36	12314	12312	12310		
	533.30	380	18746	37				12323	12323
	534.26	100	18712	38(na)					
	535.40	50	18671	39	12405	12403	12409	12397	12386
	535.94	140	18654	40	12422	12414	12418		
	536.44	380	18636	41				12433	12431
$^4F_{9/2}$	621.95	170	16074	56	15002		15005		
	622.68	185	16055	57	15021		15027	15017	15023
	623.36	174	16038	58	15038		15034		
	623.90	155	16024	59				15045	15051
	624.58	280	16006	60				15063	15054
	625.41	210	15985	61	15091		15090		
	625.82	65	15973	62				15096	15096
	625.62	210	15978	63	15098		15105		
	626.56	45	15956	64				15113	15113
$^4S_{3/2}$	769.88	280	12979	65				18090	18095
	770.06	870	12983	66	18093		18087		
	770.90	1240	12961	67				18108	18101
	771.09	480	12963	68	18113		18113		

[a](b) indicates broad band, (s) shoulder, (na) not assigned. Calculated values from C_{3v} site symmetry fits presented in Tables 2 and 3.

#171375 - $15.00 USD Received 26 Jun 2012; revised 25 Jul 2012; accepted 27 Jul 2012; published 1 Aug 2012

The first reassignment occurs in the $^4I_{15/2}$ manifold. Fluorescence spectra of Er^{3+} in the principal site for several different wavelengths in its excitation spectrum indicate that the 1558.25 nm fluorescence line's intensity at the lowest temperatures is weak and inconsistent, though as the temperature is increased it grows rapidly, as exemplified in Fig. 2. This supports [16]'s prediction of hot bands at about that wavelength, but calls into question its assignment of an energy level at 98 cm^{-1} based on this line. However, a moderately weak fluorescence line at 1544.5 nm is much more consistent for different principal site excitation wavelengths and its intensity varies only weakly with temperature, as can be seen in Fig. 2. This is much more consistent with expectations for a transition from the lowest $^4I_{13/2}$ level. On the basis of this transition, we conclude that the fourth energy level in $^4I_{15/2}$ is not at 98 cm^{-1}, but rather is at 43 cm^{-1}.

The other reassignments resulting from our refined site selection spectra involve $^4I_{11/2}$ states. A detailed excitation spectrum of the principal site fluorescence refines the energy of the transition reported as 10108 cm^{-1} in [16] to 10105 cm^{-1}, and reveals three additional excitation transitions at 10150, 10170 and 10187 cm^{-1}. The final two of these agree satisfactorily with energy levels assigned from the CL data, but the transition energies 10105 and 10150 cm^{-1} cannot plausibly be associated with any CL feature. In addition, the crystal field modeling to be reported in a later section cannot account for these features if they represent ground state absorption.

The existence of $^4I_{15/2}$ states at 43 and 135 cm^{-1} suggests explanations for these excitation lines in terms of hot band absorption. The 10105 cm^{-1} line is satisfactorily consistent with a transition from the level at 135 cm^{-1} to that observed in CL at 10237 cm^{-1}, and 10150 cm^{-1} is consistent with a transition between the levels at 43 and 10193 cm^{-1}. We conclude that the $^4I_{11/2}$ levels observed by site selection spectroscopy are the five given in column 7 of Table 1.

Figure 3 includes peaks 1 through 14 from the 12 K CL spectrum that represent transitions from the lower Stark level of $^2P_{3/2}$ to the ground state manifold $^4I_{15/2}$. Peak 1 is a shoulder that represents the transition from the initiating Stark level in $^2P_{3/2}$ at 31076 cm^{-1} to the ground state Stark level of Er^{3+} in the "a" site (Table 1). Peak 2 consists of two unresolved transitions, one transition from the initiating Stark level in $^2P_{3/2}$ at 31069 cm^{-1} to the ground state Stark level of Er^{3+} in the "b" site and a second transition from the initiating Stark level of Er^{3+} in the "a" site to the first excited Stark level at approximately 7 cm^{-1}. This analysis of the splitting is confirmed by the site selection data in Table 1 (column 7) for Er^{3+} in the "a" site. The overlap of these peaks requires deconvolution of the spectra for peaks 1 and 2. The uncertainty in separation between peaks is less than a wave number, so that in Table 1 we list the energy for both transitions as 31069 cm^{-1}. To further support this assignment we have observed emission spectra from $^4S_{3/2}$ to $^4I_{15/2}$ for Er^{3+} in the "a" site that unambiguously identifies the 7 cm^{-1} splitting between the ground state and the first excited Stark level. Emission peaks at 321.9 nm and 322.14 nm in Table 1 are very weak. They establish Stark levels at 30 cm^{-1} and 43 cm^{-1}, respectively, that are confirmed by site selection spectroscopy. The emitting level of the "b" site can also be established from energy differences from that site to lower energy Stark levels established from emission by $^4S_{3/2}$.

The CL emission spectra shown in Fig. 4 for peaks 42 through 55 were analyzed as transitions from both Stark levels of $^4S_{3/2}$ to the Stark levels of the $^4I_{15/2}$ manifold for Er^{3+} in both sites. The figure includes detector noise due to the narrow slits required to resolve the transitions observed from the two emitting Stark levels of the $^4S_{3/2}$ manifold in both sites to eight expected terminal Stark levels of $^4I_{15/2}$. Analysis of the CL spectrum confirms all eight Stark levels of the $^4I_{15/2}$ manifold reported in both sites in Table 1. The splitting of the $^4S_{3/2}$ manifold is 20 cm^{-1} (site "a") and 18 cm^{-1} (site "b"). This splitting is shown in Fig. 5 and Table 1. We list only emission from $^2P_{3/2}$ in Table 1 since the emission from $^4S_{3/2}$ simply confirms the splitting of the ground state manifold.

#171375 - $15.00 USD Received 26 Jun 2012; revised 25 Jul 2012; accepted 27 Jul 2012; published 1 Aug 2012

Perhaps the simplest spectra analyzed that demonstrate the dominance of two Er^{3+} sites in this crystal are the spectra shown in Fig. 5, representing the sharp, well defined transitions from the lower Stark level of $^2P_{3/2}$ to the two Stark components of $^4S_{3/2}$. The four peaks (65 through 68) identify the splitting of the $^4S_{3/2}$ in the "a" and "b" sites and provide the energies for the emitting Stark levels used to analyze the crystal-field splitting of the $^4I_{15/2}$ manifold described in the preceding paragraph. The difference in energy between the multiplet barycenters of $^4S_{3/2}$ of Er^{3+} in the "a" and "b" sites is comparable to the energy shift found between the ground-state Stark level of Er^{3+} in both sites as well, suggesting the impurity traps represented by these two sites have nearly the same depth.

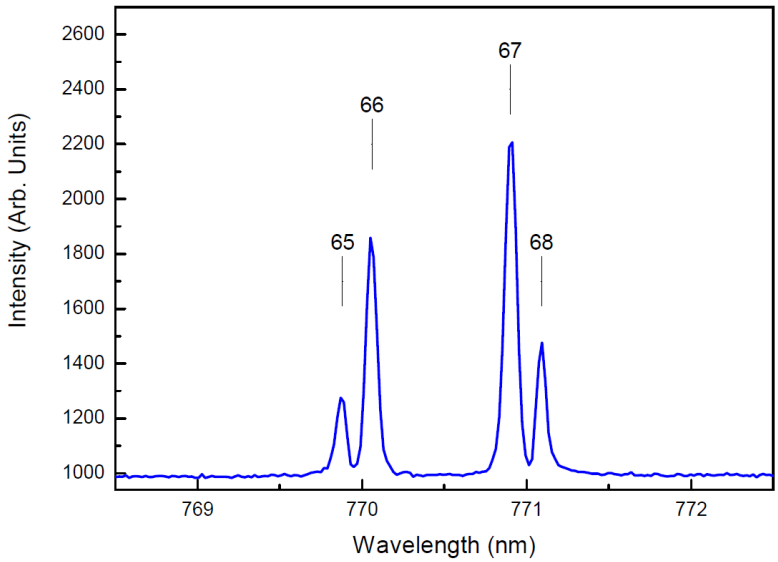

Fig. 5. The 12 K CL spectrum of Er^{3+} in AlN between 768 nm and 773 nm representing transitions from $^2P_{3/2}$ to $^4S_{3/2}$.

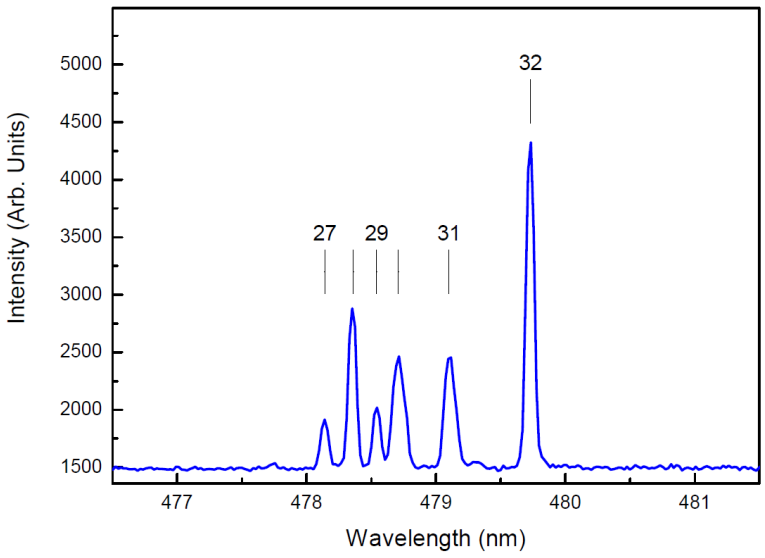

Fig. 6. The 12 K CL spectrum of Er^{3+} in AlN between 476 nm and 482 nm representing transitions from $^2P_{3/2}$ to $^4I_{11/2}$.

#171375 - $15.00 USD Received 26 Jun 2012; revised 25 Jul 2012; accepted 27 Jul 2012; published 1 Aug 2012

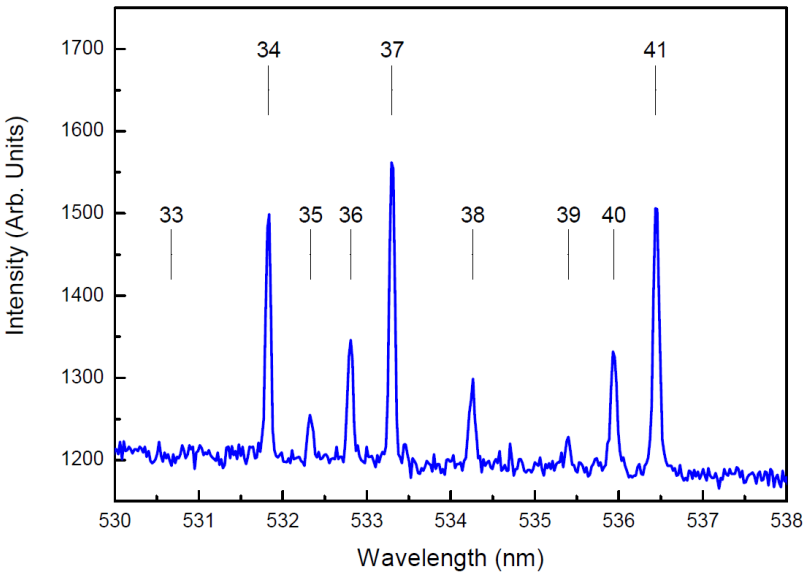

Fig. 7. The 12 K CL spectrum of Er^{3+} in AlN between 530 nm and 538 nm representing transitions from $^2P_{3/2}$ to $^4I_{9/2}$.

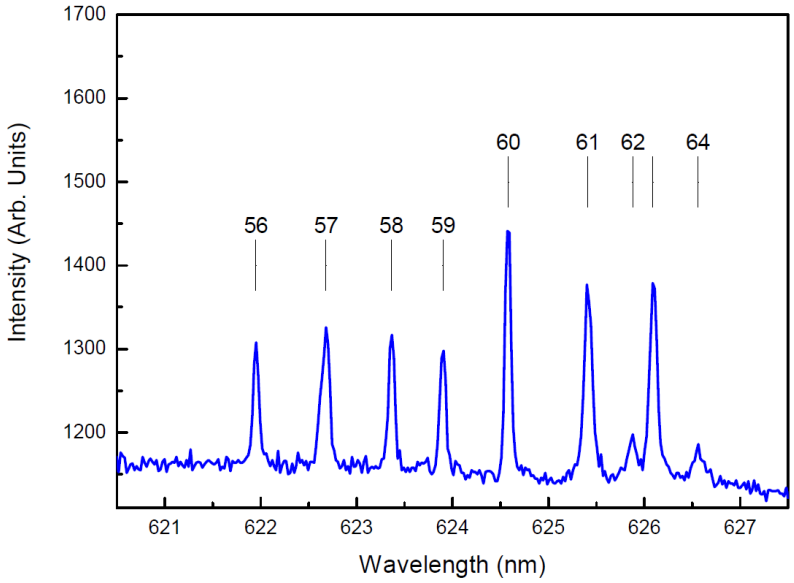

Fig. 8. The 12 K CL spectrum of Er^{3+} in AlN between 620.5 nm and 627.5 nm representing transitions from $^2P_{3/2}$ to $^4F_{9/2}$.

The spectra representing transitions from $^2P_{3/2}$ to $^4I_{11/2}$ are shown in Fig. 6. At first glance, it appears that exactly $J + 1/2$ expected peaks (27 through 32) are observed for a single site. However, a closer look indicates that each peak appears to have a discernible shoulder, suggesting that the peaks may be deconvoluted into two peaks with nearly the same energy. The results from deconvolution suggest the experimental Stark levels for this manifold for the "a" and "b" sites reported in Table 1. Stark levels 10192 cm^{-1} and 10211 cm^{-1} in the "a" site are similar to levels assigned by analysis of the site selection spectra. The experimental Stark levels for $^4I_{11/2}$ of Er^{3+} in both sites are also in reasonable agreement with calculated energy

#171375 - $15.00 USD Received 26 Jun 2012; revised 25 Jul 2012; accepted 27 Jul 2012; published 1 Aug 2012

values listed in columns 8 and 10 of Table 1 that are based on the modeling studies described in the following section.

Figures 7 and 8 show the 12 K CL emission spectra representing transitions from $^2P_{3/2}$ to $^4I_{9/2}$, and $^2P_{3/2}$ to $^4F_{9/2}$, respectively. The transitions are represented by peaks 33 through 41 and peaks 56 through 64. Peak 33 is very weak and broad, and probably represents two separate transitions observed in the spectrum between 530 and 531 nm. In Fig. 7, five strong peaks can be assigned to transitions that identify five Stark levels within the $^4I_{9/2}$ "a" site manifold based on comparison with levels determined by site selection spectra listed in column 7 of Table 1. The remaining peaks and terminal Stark levels are identified with the "b" site, with the exception of peak 38 which is presently unassigned. In Fig. 8, nine peaks and a shoulder (on peak 54) are observed and ten terminal Stark levels are expected from the $^2P_{3/2}$ to $^4F_{9/2}$ in those sites.

Five of these transitions were assigned to the "a" site and the remaining five to the "b" site using methods of energy differences. Peaks in both figures are sharp and relatively intense, and limited by spectral resolution of the spectrograph, suggesting they may have relatively large emission cross sections. The difference in manifold splitting of $^4I_{9/2}$ and $^4F_{9/2}$ provides an important distinction between sites in the subsequent modeling studies of the crystal-field splitting of these states.

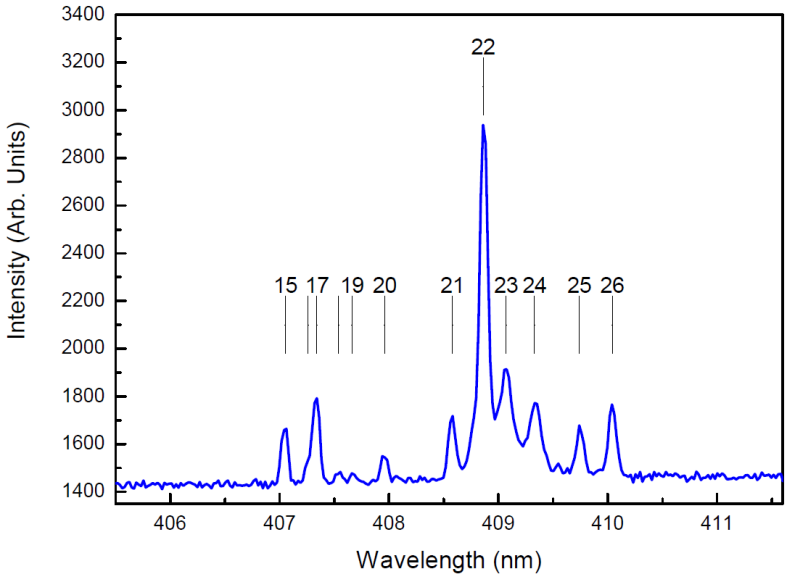

Fig. 9. The 12 K CL spectrum of Er^{3+} in AlN between 405.5 nm and 411.5 nm representing transitions from $^2P_{3/2}$ to $^4I_{13/2}$.

The CL emission spectra, representing transitions from $^2P_{3/2}$ to $^4I_{13/2}$ (levels 15 through 26 in Fig. 9), are perhaps the most difficult to analyze in the entire set of data given the number of similar energy differences between Stark levels and the inhomogeneous broadening of the peaks. Ambiguity is greatly reduced by comparing the peaks and transitions that give the experimental energy level scheme of Stark levels selected for the "a" site in Table 1 (column 6) with the experimental Stark levels for the $^4I_{13/2}$ manifold analyzed from the site selection spectroscopy. The remaining peaks and subsequent terminal Stark levels then can be assigned by process of elimination to Stark levels of Er^{3+} in the "b" site, in column 9 of Table 1. The experimental Stark levels expected for $^4I_{13/2}$ for Er^{3+} in both "a" and "b" sites in Table 1 agree well with the assignments made from the site selection spectroscopy and with the results of the crystal-field modeling studies reported in the next section.

#171375 - $15.00 USD Received 26 Jun 2012; revised 25 Jul 2012; accepted 27 Jul 2012; published 1 Aug 2012

4. Modeling the crystal field splitting

The 34 identified experimental Stark levels for each of the two principle ("a" and "b") sites, representing every Stark component of the seven lowest-energy multiplet manifolds of Er^{3+} along with the lowest Stark component of the emitting $^2P_{3/2}$ multiplet in single-crystal hexagonal phase AlN, are reported in Tables 2 and 3 for the main "a" and "b" sites, respectively. These energy levels are modeled using a parameterized Hamiltonian written in standard practice [29,30] that consists of spherically symmetric "atomic" contributions given by,

$$H_{\mathrm{A}} = E_{avg} + \sum_k F^k \,\mathrm{f}_k + \alpha\,\mathrm{L}(\mathrm{L}+1) + \beta\,\mathrm{G}(G_2) + \gamma\,\mathrm{G}(R_7) + \sum_i T^i \,\mathrm{t}_i + \varsigma_{so}\,\mathrm{A}_{so} + \sum_k P^k \,\mathrm{p}_k + \sum_j M^j \,\mathrm{m}_j \tag{1}$$

and non-spherically-symmetric contributions from the one electron crystal field,

$$H_{\mathrm{cf}} = \sum_{k,q} B_q^k C_q^{(k)}. \tag{2}$$

In C_{3v} symmetry there are six independent B_q^k crystal-field parameters: B_0^2, B_0^4, B_3^4, B_0^6, B_3^6, and B_6^6. When C_3 symmetry is considered, each of the three $q \neq 0$ parameters are allowed to be complex, which is conventionally written in real plus imaginary terms as, $B_q^k + iS_q^k$, resulting in nine crystal-field parameters. However, it is well-known that any one of the imaginary terms may be set equal to zero by appropriate rotation about the parametrization z-axis, with standard convention setting $S_3^4 = 0$. This results in eight *independent* crystal-field parameters in C_3 symmetry. For C_{1h} symmetry, there are 15 allowed crystal-field parameters: B_0^2, $B_2^2 + iS_2^2$, B_0^4, $B_2^4 + iS_2^4$, $B_4^4 + iS_4^4$, B_0^6, $B_2^6 + iS_2^6$, $B_4^6 + iS_4^6$, and $B_6^6 + iS_6^6$. As with C_3 symmetry, one of the 15 crystal-field parameters can be set to zero via appropriate rotation about the parametrization z-axis, with standard convention setting $S_2^2 = 0$. This results in 14 *independent* crystal-field parameters in C_{1h} symmetry. The experimental Stark levels are modeled through use of a Monte Carlo method [31,32] in which each of the independent crystal-field parameters is given random starting values between −1000 and + 1000 cm^{-1} and optimized using standard least-squares fitting between calculated and experimental levels.

Based on 34 Stark levels for each site and assuming C_{3v} site symmetry for the Er^{3+} ion, the final overall standard deviation between calculated-to-experimental Stark levels for site "a" is 8.7 cm^{-1} (rms error = 7.0 cm^{-1}) and for the same number of Stark levels for site "b", the overall standard deviation is 8.3 cm^{-1} (rms error = 6.7 cm^{-1}). Table 2, columns 4-7 compare the modeling results for site "a" with experimental energy values given in column 2. Calculated irreducible representations (irreps) ($\Gamma_{1/2}$ and $\Gamma_{3/2}$) and the largest M_J components are given for each doublet level as determined by the best fit of the data to C_{3v} symmetry. The results for site "b" are given in Table 3 using the same format as for Table 2. The atomic and crystal-field parameters that are used to obtain these results are given in Table 4. Six of the 20 atomic parameters were allowed to vary in the fitting process, along with all six crystal-field parameters. Parameter uncertainties for these twelve parameters are given in parentheses after the parameter values. The other 14 atomic parameters were held fixed at previously determined values. Stark levels calculated using these parameters are also given in Table 1, columns 8 and 10.

When we carried out the modeling calculations assuming C_3 site symmetry for the Er^{3+} ion, there was no significant improvement in the calculated-to-experimental fitting, with higher standard deviations for both the site "a" and "b" fittings.

#171375 - $15.00 USD Received 26 Jun 2012; revised 25 Jul 2012; accepted 27 Jul 2012; published 1 Aug 2012

Table 2. Crystal-field splitting for energy levels of site "a" of Er^{3+}:AlN using wavefunctions of C_{3v} and C_{1h} symmetry

			C_{3v} Symmetry				C_{1h} Symmetry		
$^{2S+1}L_J$	Doublet Level	E_{exp} (cm^{-1})	Irrep (Γ)	M_J [a]	E_{calc} (cm^{-1})	ΔE (cm^{-1})	M_J [a]	E_{calc} (cm^{-1})	ΔE (cm^{-1})
$^4I_{15/2}$	1	0	1/2	±11/2	–6	6	±13/2	–3	3
	2	7	3/2	±9/2	9	–2	±5/2	12	–5
	3	30	1/2	±7/2	41	–11	±11/2	36	–6
	4	43	1/2	±13/2	56	–13	±13/2	50	–7
	5	138	1/2	±11/2	128	10	±9/2	132	6
	6	191	3/2	±9/2	180	11	±15/2	183	8
	7	239	1/2	±7/2	247	–8	±15/2	237	2
	8	272	3/2	±15/2	272	0	±3/2	280	–8
						$\sigma = 8.8$ [b]			$\sigma = 6.1$ [b]
$^4I_{13/2}$	9	6516	3/2	±9/2	6512	4	±7/2	6512	4
	10	6528	1/2	±1/2	6523	5	±9/2	6520	8
	11	6533	1/2	±7/2	6527	6	±5/2	6536	–3
	12	6553	1/2	±11/2	6567	–14	±11/2	6558	–5
	13	6608	3/2	±3/2	6601	7	±7/2	6603	5
	14	6625	1/2	±1/2	6625	0	±13/2	6625	0
	15	6677	1/2	±13/2	6664	13	±3/2	6663	14
						$\sigma = 8.3$			$\sigma = 6.7$
$^4I_{11/2}$	16	10167	1/2	±7/2	10169	–2	±7/2	10167	0
	17	10177	3/2	±9/2	10173	4	±9/2	10175	2
	18	10185	1/2	±5/2	10181	4	±9/2	10182	3
	19	10192	3/2	±3/2	10203	–11	±5/2	10203	–11
	20	10211	1/2	±1/2	10216	–5	±11/2	10218	–7
	21	10237	1/2	±11/2	10243	–6	±1/2	10241	–4
						$\sigma = 6.3$			$\sigma = 5.9$
$^4I_{9/2}$	22	12238	1/2	±7/2	12229	9	±7/2	12230	8
	23	12279	1/2	±1/2	12285	–6	±3/2	12279	0
	24	12314	3/2	±3/2	12310	4	±1/2	12314	0
	25	12405	3/2	±9/2	12409	–4	±5/2	12397	8
	26	12422	1/2	±5/2	12418	4	±3/2	12430	–8
						$\sigma = 5.8$			$\sigma = 6.3$
$^4F_{9/2}$	27	15002	1/2	±7/2	15005	–3	±5/2	15003	–1
	28	15021	3/2	±9/2	15027	–6	±7/2	15025	–4
	29	15038	1/2	±5/2	15034	4	±3/2	15043	–5
	30	15091	3/2	±3/2	15090	1	±3/2	15090	1
	31	15098	1/2	±1/2	15105	–7	±9/2	15101	–3
						$\sigma = 4.6$			$\sigma = 3.1$
$^4S_{3/2}$	32	18093	3/2	±3/2	18087	6	±1/2	18091	2
	33	18113	1/2	±1/2	18113	0	±3/2	18108	5
						$\sigma = 4.5$			$\sigma = 3.6$
$^2P_{3/2}$	77	31076	3/2	±3/2	31076	0	±1/2	31076	0
	78	—	1/2	±1/2	31136		±3/2	31114	

[a]The largest M_J component to the Stark level wave function.
[b]The rms deviation for each multiplet in cm^{-1}.

Modeling calculations using C_{1h} site symmetry showed a modest improvement in the fittings, with the standard deviation for the site "b" fitting decreasing from 8.3 to 7.6 cm^{-1} (rms error decreasing from 6.7 to 4.9 cm^{-1}). For the site "a" fitting, the standard deviation was almost unchanged (going from 8.7 to 8.8 cm^{-1}), though the rms error decreased from 7.0 to 5.7 cm^{-1}. The right-hand columns of Tables 2 and 3 present the energy level calculations using C_{1h} symmetry. As can be seen from these two tables, the additional crystal-field parameters allowed in C_{1h} symmetry improve the energy level calculations for specific levels of $^4I_{15/2}$ and $^4I_{13/2}$ multiplets.

#171375 - $15.00 USD Received 26 Jun 2012; revised 25 Jul 2012; accepted 27 Jul 2012; published 1 Aug 2012

Table 3. Crystal-field splitting for energy levels of site "b" of Er^{3+}:AlN using wavefunctions of C_{3v} and C_{1h} symmetry

			C_{3v} Symmetry				C_{1h} Symmetry		
$^{2S+1}L_J$	Doublet Level	E_{exp} (cm^{-1})	Irrep (Γ)	M_J [a]	E_{calc} (cm^{-1})	ΔE (cm^{-1})	M_J [a]	E_{calc} (cm^{-1})	ΔE (cm^{-1})
$^4I_{15/2}$	1	0	1/2	±13/2	0	0	±7/2	1	–1
	2	56	1/2	±11/2	56	0	±9/2	53	3
	3	131	3/2	±9/2	124	7	±11/2	123	8
	4	147	1/2	±1/2	137	10	±13/2	142	5
	5	172	3/2	±3/2	174	–2	±15/2	173	–1
	6	200	1/2	±5/2	200	0	±15/2	202	–2
	7	248	1/2	±7/2	250	–2	±13/2	253	–5
	8	285	3/2	±15/2	300	–15	±1/2	294	–9
						σ = 6.9 [b]			σ = 5.0 [b]
$^4I_{13/2}$	9	6520	1/2	±11/2	6518	2	±5/2	6518	2
	10	6546	3/2	±9/2	6551	–5	±9/2	6550	–4
	11	6575	1/2	±7/2	6580	–5	±7/2	6581	–6
	12	6601	1/2	±1/2	6605	–4	±13/2	6602	–1
	13	6618	3/2	±3/2	6622	–4	±11/2	6615	3
	14	6630	1/2	±5/2	6629	1	±13/2	6633	–3
	15	6688	1/2	±13/2	6666	22	±1/2	6673	15
						σ = 9.1			σ = 6.6
$^4I_{11/2}$	16	10164	3/2	±9/2	10166	–2	±5/2	10165	–1
	17	10185	1/2	±7/2	10184	1	±3/2	10181	4
	18	10192	1/2	±5/2	10198	–6	±7/2	10192	0
	19	10209	1/2	±1/2	10210	–1	±9/2	10209	0
	20	10213	3/2	±3/2	10213	0	±11/2	10212	1
	21	10230	1/2	±11/2	10229	1	±1/2	10238	–8
						σ = 2.6			σ = 3.7
$^4I_{9/2}$	22	12235	1/2	±7/2	12233	2	±5/2	12241	–6
	23	12289	1/2	±1/2	12301	–12	±3/2	12292	–3
	24	12323	3/2	±3/2	12323	0	±1/2	12326	–3
	25	12397	1/2	±5/2	12386	11	±7/2	12392	5
	26	12433	3/2	±3/2	12431	2	±1/2	12425	8
						σ = 7.4			σ = 5.5
$^4F_{9/2}$	27	15017	1/2	±5/2	15023	–6	±7/2	15017	0
	28	15045	1/2	±7/2	15051	–6	±9/2	15044	1
	29	15063	3/2	±3/2	15054	9	±1/2	15063	0
	30	15096	3/2	±9/2	15096	0	±3/2	15100	–4
	31	15113	1/2	±1/2	15113	0	±1/2	15114	–1
						σ = 5.5			σ = 1.7
$^4S_{3/2}$	32	18090	1/2	±1/2	18095	–5	±3/2	18084	6
	33	18108	3/2	±3/2	18101	7	±1/2	18112	–4
						σ = 6.3			σ = 5.0
$^2P_{3/2}$	77	31069	1/2	±1/2	31069	0	±3/2	31069	0
	78	—	3/2	±3/2	31078		±1/2	31121	

[a]The largest M_J component to the Stark level wave function.
[b]The rms deviation for each multiplet in cm^{-1}.

#171375 - $15.00 USD Received 26 Jun 2012; revised 25 Jul 2012; accepted 27 Jul 2012; published 1 Aug 2012

Table 4. Calculated atomic and crystal-field parameters in C_{3v} symmetry for Er^{3+}:AlN

Parameter	Site "a" value (cm^{-1})	Site "b" value (cm^{-1})
E_{avg}	35445 (21)[a]	35372 (9)[a]
F_2	97756 (168)	97192 (56)
F_4	66788 (188)	66983 (107)
F_6	56908 (281)	55923 (121)
α	29.2	29.2
β	–911	–911
γ	1800	1800
ζ	2369 (2)	2365 (2)
T_2	400	400
T_3	45	45
T_4	71	71
T_6	–299	–299
T_7	277	277
T_8	419	419
M_0	5.67 (0.24)	5.58 (0.18)
M_2	0.56 M_0	0.56 M_0
M_4	0.38 M_0	0.38 M_0
P_2	922	922
P_4	0.75 P_2	0.75 P_2
P_6	0.50 P_2	0.50 P_2
B_0^2	246 (41)	–73 (32)
B_0^4	759 (87)	638 (62)
B_3^4	±417 (54)	±408 (83)
B_0^6	268 (45)	541 (23)
B_3^6	∓ 293 (28)	±213 (36)
B_6^6	–329 (30)	116 (25)
N	34	34
σ	8.7	8.3
rms	7.0	6.7

[a]Values in parenthesis indicate uncertainties (in cm^{-1}) in the fitted parameters; other parameters were held fixed.

Table 5 presents the C_{1h} crystal-field parameters determined for both sites "a" and "b". For comparison, the C_{3v} parameters, transformed to the coordinate system used by the C_{1h} parametrization by Euler rotations α = 90°, β = 90°, are given to the left of the C_{1h} parameters for each site. The fitting improvement using C_{1h} parameters is statistically significant, indicating that the true site symmetry for both the "a" and "b" sites is most likely C_{1h}. However, as can be seen from Table 5, the uncertainties in the values of the C_{1h} crystal-field parameters are large, and in most cases are larger than the difference between the C_{3v} and the C_{1h} parameter values. The large parameter value uncertainties means that the wavefunctions generated by the C_{1h} Hamiltonian will be less reliable for the purposes of deducing other properties of the systems, such as calculated Zeeman splittings. The relatively small differences between the C_{3v} and the C_{1h} parameter values indicate that it is reasonable to use an approximate C_{3v} symmetry to model these systems.

Using wavefunctions generated from the C_{3v} modeling studies for both sites, we calculated the Zeeman splitting and g-factors for the Stark levels of the ground $^4I_{15/2}$ manifold. The Zeeman splitting calculated for an external magnetic field of 0.15 T, along with resulting calculated g-values ($g_{\|}$ and $g_{\perp}$), are listed in Table 6 for site "a" and in Table 7 for site "b". We have compared these calculated results with experimental values for $g_{\|}$ and $g_{\perp}$ obtained from an investigation of the EPR spectrum on single-crystal Er^{3+} in AlN [14]. Only one Er^{3+} site was observed in the EPR study, with experimental g-values for the ground state Stark level reported as $g_{\|}$ = 4.337 and $g_{\perp}$ = 7.647. The experimental g-values agree with the

#171375 - $15.00 USD Received 26 Jun 2012; revised 25 Jul 2012; accepted 27 Jul 2012; published 1 Aug 2012

calculated values $g_{\|} = 5.5$ and $g_{\perp} = 6.1$ given in Table 6 for site "a", and do not agree with the calculated values $g_{\|} = 14.7$ and $g_{\perp} = 1.0$ given in Table 7 for site "b". We therefore conclude that the Er^{3+} ions occupy site "a" in the dilute sample used for the EPR study.

Table 5. Calculated crystal-field parameters, comparing C_{3v} symmetry calculations with C_{1h} symmetry for Er^{3+}:AlN

Parameter	Site "a" value (cm^{-1})[a]		Site "b" value (cm^{-1})[a]	
	C_{3v}	C_{1h}	C_{3v}	C_{1h}
B_0^2	−123	−5 (108)[b]	37	64 (73)[b]
B_2^2	150	136 (43)	−45	−190 (31)
B_0^4	285	538 (197)	239	345 (171)
B_2^4	−300	−371 (135)	−252	232 (110)
S_2^4	−390	−214 (141)	−382	−256 (132)
B_4^4	397	353 (141)	334	383 (85)
S_4^4	−147	−117 (215)	−144	52 (288)
B_0^6	229	195 (117)	−279	−281 (55)
B_2^6	315	110 (113)	93	−37 (68)
S_2^6	−165	−134 (75)	120	79 (58)
B_4^6	−10	−119 (146)	−219	−161 (120)
S_4^6	201	206 (87)	−146	−158 (120)
B_6^6	138	84 (312)	253	306 (67)
S_6^6	136	353 (75)	−99	56 (329)
N	34	34	34	34
σ	8.7	8.8	8.3	7.6
rms	7.0	5.7	6.7	4.9

[a]C_{3v} parameter values have been determined from parameters given in Table 4 by Euler rotations $\alpha = 90°$, $\beta = 90°$.
[b]Values in parenthesis indicate uncertainties (in cm^{-1}) in fitted parameters.

Table 6. Splitting of "a" site crystal-field energy levels of Er^{3+}:AlN in a 0.15 T magnetic field (in cm^{-1}), and resultant *g*-values for the ground multiplet $^4I_{15/2}$

$^{2S+1}L_J$	Energy Level (cm^{-1})	Doublet Level	Irrep (Γ)	Magnetic field ∥ c-axis			Magnetic field ⊥ c-axis		
				ΔE_{calc}	g_{calc}	g_{exp}[a]	ΔE_{calc}	g_{calc}	g_{exp}[a]
$^4I_{15/2}$	0	1	1/2	0.38	5.5	4.337	0.43	6.1	7.647
	7	2	3/2	0.47	6.7	—	0.00	0.0	—
	30	3	1/2	0.19	2.7	—	0.43	6.2	—
	43	4	1/2	0.83	11.9	—	0.29	4.1	—
	138	5	1/2	0.36	5.1	—	0.34	4.8	—
	191	6	3/2	0.49	6.9		0.00	0.0	
	239	7	1/2	0.14	2.0	—	0.62	8.9	—
	272	8	3/2	1.10	15.7	—	0.00	0.0	—

[a]Experimental values from [14].

#171375 - $15.00 USD Received 26 Jun 2012; revised 25 Jul 2012; accepted 27 Jul 2012; published 1 Aug 2012

Table 7. Splitting of "b" site crystal-field energy levels of Er^{3+}:AlN in a 0.15 T magnetic field (in cm^{-1}), and resultant *g*-values for the ground multiplet $^4I_{15/2}$

$^{2S+1}L_J$	Energy Level (cm^{-1})	Doublet Level	Irrep (Γ)	Magnetic field ∥ c-axis			Magnetic field ⊥ c-axis		
				ΔE_{calc}	g_{calc}	g_{exp}	ΔE_{calc}	g_{calc}	g_{exp}
$^4I_{15/2}$	0	1	1/2	1.03	14.7	—	0.07	1.0	—
	56	2	1/2	0.82	11.7	—	0.04	0.5	—
	131	3	3/2	0.62	8.9	—	0.00	0.0	—
	147	4	1/2	0.03	0.5	—	0.65	9.2	—
	172	5	3/2	0.09	41.3	—	0.00	0.0	—
	200	6	1/2	0.12	1.8	—	0.55	7.9	—
	248	7	1/2	0.30	14.3	—	0.56	8.0	—
	285	8	3/2	1.14	16.2	—	0.00	0.0	—

5. Summary and conclusions

With support from analyses of site-selective spectroscopy, the cathodoluminescence (CL) spectra of $Er^{3+}(4f^{11})$ in single-crystal hexagonal phase of AlN have been assigned to two principal sites in the lattice. The 12 K CL spectrum obtained between 320 nm and 775 nm was analyzed for the $J + 1/2$ Stark levels of the ground-state $^4I_{15/2}$ and excited state $^4I_{13/2}$, $^4I_{11/2}$, $^4I_{9/2}$, $^4F_{9/2}$, and $^4S_{3/2}$ multiplet manifolds. The emission to the Stark levels of these manifolds came from the lower-energy Stark level of the $^2P_{3/2}$ multiplet, with additional data coming from the $^4S_{3/2} \rightarrow {}^4I_{15/2}$ emission. More than 97% of the observed CL spectra were accounted for in terms of the two principal sites. More than 65 peaks and shoulders were evaluated and a number of deconvolution studies were carried out on problematic features.

A crystal-field splitting calculation was carried out for each site using a parameterized Hamiltonian that included atomic and crystal-field terms for states of $Er^{3+}(4f^{11})^{2S+1}L_J$. The identification of two Er^{3+} sites in AlN suggested a descent in symmetry calculation from C_{3v} to C_{1h} for each site, since Er^{3+} has a larger ionic radius than Al^{3+}, and is expected to cause stress on the surrounding environment, especially when doped into AlN in sufficient quantities to observe the optical spectrum of the $4f \rightarrow 4f$ transitions. Likewise, Er^{3+} may substitute for a basal-plane N to form complexes such as Er^{3+}-O_N or Er^{3+}-V_N with C_{1h} symmetry. Er^{3+} ions in Al^{3+} sites may shift along the c-axis toward the basal plane into a site of C_{1h} symmetry to lower the energy of Er^{3+} as a trap impurity in AlN. The modeling of the Er^{3+} site symmetry gave interesting results, as shown in Table 5. For site "a" the C_{1h} crystal-field fitting gave a slightly higher standard deviation than obtained for C_{3v} symmetry, while for site "b" the C_{1h} fitting gave a statistically-significant lower standard deviation than for C_{3v} symmetry. However, for most of the crystal-field parameters given in Table 5, the difference between the C_{3v} and C_{1h} symmetry parameter values is less than the statistical uncertainty in the C_{1h} symmetry crystal-field parameters. Therefore, we conclude that C_{3v} remains a reasonable approximate symmetry for Er^{3+} ions in both sites of AlN, and that wavefunctions generated using the assumption of C_{3v} symmetry may be used reasonably for calculation of other optical properties, such as Zeeman splittings of the states.

#171375 - $15.00 USD Received 26 Jun 2012; revised 25 Jul 2012; accepted 27 Jul 2012; published 1 Aug 2012